# Refined Element Discontinuous Numerical Analysis of Dry–Contact Masonry Arches

J.L. Pérez–Aparicio[a,*], R. Bravo[b,1], P. Ortiz[b,1]

[a]*Department of Continuum Mechanics and Theory of Structures, Universitat Politècnica de València 46022 Valencia, Spain*
[b]*University of Granada, Esc. Ing. Caminos. Campus Fuentenueva. 18071 Granada, Spain*

## Abstract

The behavior of buried masonry arches is studied in this article using the Discontinuous Deformation Analysis (DDA), a numerical method that allows for the physical simulation of the intrinsic structure discontinuities since it is based on contact and friction among pseudo–rigid blocks. Two types of arches (or vaults) are studied with a specially developed computer program, one of semicircular and another of ovoidal shape. The loads are self–weight, lateral filling, embankment thrusts and concentrated (through a short distribution) forces close to the peak. These loads are transformed into point forces applied to the center of gravity of each block with simple formulae from classical mechanics. Equilibrium is reached in the whole structure through contact forces calculated with a standard contact algorithm: penalty plus Coulomb friction.

DDA–macroblocks composed of linked (through penalty contact springs)

---

[*]Corresponding author. Tel. +34963877000 (Ext. 71815)
*Email addresses:* `jopeap@mes.upv.es` (J.L. Pérez–Aparicio), `rbravo@ugr.es` (R. Bravo), `portiz@ugr.es` (P. Ortiz)
[1]Tel. +34958249960

pseudo–rigid blocks are formulated. This linkage allows for the simulation of collapse by instability or by stress compressive failure more accurately than traditional DDA analyses, for instance funicular polygons.

The numerical results are compared with those of the experiments taken from the literature with, for most cases, very good agreement given the uncertainties on geometry and material properties and given the intrinsic quality dispersion of masonry structures. Collapse loads as function of number of joints, safety factors and limit point forces from the numerical and experimental results are compared. The hinges that appear prior to collapse are also compared, obtaining again for most cases very good agreement.

## 1. Introduction

There exist a large building and civil structure heritage in many countries to be evaluated, maintained and preserved. In particular, masonry arches are one of the most ancient structural solutions, probably due to their simple geometry and construction and their intrinsic capability of making its material to work in compression. Masonry structures in general are composed of blocks whose stability is achieved by direct dry contact and friction among each other, or indirectly through a thin interface of elastoplastic material. Therefore, as a consequence of contact they show complex nonlinear and discontinuous behavior; analytical formulations or graphical methods are not able to completely model such behavior and it is necessary to use numerical even for the simplest geometries and loads.

2

The masonry arch as an architectonic solution was already widespread during roman times for above-ground or buried buildings, for which the structure is subjected to lateral thrust; the romans even constructed very large vaults (longitudinal arches) or domes without semicircular shape. The first attempts to analyze the behavior of masonry could date from the early experimental works of Vitrubio in the first century B.C. Many years later, others were focused on stability analysis, Leonardo da Vinci (circa 1500). But only at the beginning of the XIX century geometrical methods started to be used to properly design these structures. Recently, theoretical developments such as those of the classical reference [1] considered masonry as a rigid continuum and did not take into account its weak resistance under tension or tangential stresses. Analytical methods from [2], [3] were developed during WWII to reach the maximum load carrying capacity of bridges under the weight of armored vehicles. The main shortcoming of most of the design methods, including some of the modern numerical ones, is that they consider the arch as a continuum, see [4], [5].

The pioneer articles that modeled masonry with the Finite Element Method (FEM), [6], [7], did again not consider the discontinuity of the blocks. References [8], [9] combined FEM with more advanced models based on homogenization techniques and obtained fairly good results. More advanced approaches take into account the discontinuities using contact mechanics, [10] or fracture mechanics, [11] either for static analysis or [12] for dynamic. These techniques are expensive since the number of nodes necessary to model contacts and blocks is relatively large.

Due to the possible high number of discontinuities in masonry struc-

3

tures, the Discrete Deformation Analysis (DDA) is particularly well suited for their study, see [13]. DDA can model the discontinuities simulating the more or less constant layer of mortar using the numerical contact parameters (impenetrability, friction, cohesion etc.) without the addition of new nodal unknowns although introducing non–linearities. In addition, DDA is well suited because is based on a displacement formulation more compatible with the targeted type of problems. Other methods such as the Discrete Element (DEM) or Non–Smooth Contact Dynamics, [14], [15], were designed as explicit dynamic, requiring very small time steps and artificial damping; their stability and convergence present problems for static or quasi–static cases. Both methods were applied to the dynamic analysis of masonry structures under earthquake loads, [15], [16] and [17]. The comparison between DEM and FEM approaches is discussed in [18], where the difficulties of FEM with a high number of contacts and the necessity of an accurate description of geometry and constitutive parameters for DEM are described.

The theoretical and numerical bases of DDA are well known, see [19], and here only a global introduction is given. The DDA discretization often uses only one node per block, aspect computationally attractive. But then strains and stresses are uniform inside each block, obtaining a poor representation of the internal elastic fields. The combination of DEM and FEM, [20], [21], solves this shortcoming and is able to model discontinuities although again with a high computational cost.

In the present article, the authors propose to model masonry arches with the attachment of individual subblocks composing DDA macroblocks. The technique allows to accurately capture internal deformation and stress

4

fields with a reasonable computational cost. Field experiments performed by CEBTP Solen for the french *Sociètè National des Chemins de Fer* in 1980 are described in [22], [23] and simulated here. In these experiments, the stability of two–dimensional arches with different geometries and made out of cut stone at real scale was tested with a variable number of blocks and different applied loads:

- Case 1. Filling thrust plus convoy weight, for collapse prediction as function of number of blocks

- Case 2. Filling plus embankment, for influence of embankment thickness

- Case 3. Filling plus concentrated load, for influence of load intensity

The term filling refers to soil at the sides and at the top of the arch, the latter composed of horizontal layers denominated embankment. The filling either stabilizes as in a bridge, or constitutes the terrain load as in tunnels, see [24]; the point load represents weight transmitted by, for instance, a heavy vehicle.

The results of the experiments are compared with those from the numerical simulation. In spite of the lack of statistical data (only one or two tests were performed for each configuration) and the uncertainties of the data (dimensions, material properties etc.), the numerical and experimental results are very close. These comparisons validate the applicability of discontinuous numerical methods for real curved masonry structures under several types of loads.

## 2. Masonry and contact

Masonry arches are composed of a collection of pieces in general glued at the joints by a layer of mortar with a small tensile strength but also directly in contact. The arch compensates the action of internal and external loads with contact forces at joints, creating an internal line of application of resultant forces. The equilibrium is reached when all the sections of the arch work in compression; the line crosses the central core of all sections. In any other case some sections works under medium tensile or tangential stresses, blocks slide and/or separate causing the collapse of the arch. Therefore, the design of arches must take into consideration a high strength for compressive but not for tensile or tangential stresses: the arch is aimed to optimally enforce compression.

Contact is the constitutive model that dominates this behavior and is based on two basic concepts: lack of interpenetration between blocks and frictional behavior. The first is governed by the gap function $g_N$ and the contact penalty algorithm, see Ref. [19]. The gap function measures the normal distance between every pair of opposite points of two contacting joints. In case of penetration, the contact algorithm inserts a compressive contact force $f_{cN}$ normal to the joint modeled by a high stiffness elastic spring that enforces $g_N = 0$. For $g_N > 0$, blocks are separated and $f_{cN} = 0$.

The frictional behavior is controlled by two terms: friction and cohesion. The first is represented by a tangential force $\boldsymbol{f}_r$ related to the normal $f_N$ with a coefficient $\mu = \tan\phi$ ($\phi$ is the angle of friction), or in physical terms the mechanical clinging between two pieces due to the asperities of their surfaces. The cohesion $\boldsymbol{C}$ is the magnitude of the friction force to break the joint when

the normal is null. Consequently, the total friction force is $\boldsymbol{f}_r = \mu \boldsymbol{f}_N + \boldsymbol{C}$. In case that the tangential component of resultant force exceeds $\boldsymbol{f}_r$ blocks slide and the arch collapses.

Since the tensile strength of masonry structures is almost negligible, special methods called "limit calculation" have existed for some time. They are based on the concept of "breaking joint" from Coulomb (1773), under two basic hypotheses:

- Lack of tractions in the structure, all sections under compression

- Tangential forces in the arch section lower than the friction resistance

These hypotheses are analogous to two of the standard contact conditions: Kuhn–Tucker and Coulomb friction respectively, see [25], [26]. The formulation of DDA naturally incorporates the hypotheses for any geometry or load, and provides results close to the experimental ones for the representative cases shown in the following sections.

According to the second law of the thermodynamics, a system of blocks under internal or external loadings deforms or moves so that the total energy $\Pi$ is in a minimum. DDA, see Ref. [19], is a numerical method that provides the mechanical response of a system composed by $N$ interacting bodies through the minimization of $\Pi$, energy that is defined as summation of potential $H$ and kinetic energies. For masonry, the former related to internal and external loads, strain and contact interactions. The latter is neglected since no external dynamic effects are applied, therefore $\Pi = \sum_{i=1}^{N} H_i$. The minimization of $\Pi$ respect to the discretized $n_{dg}$ degrees of freedom $D_i$ of
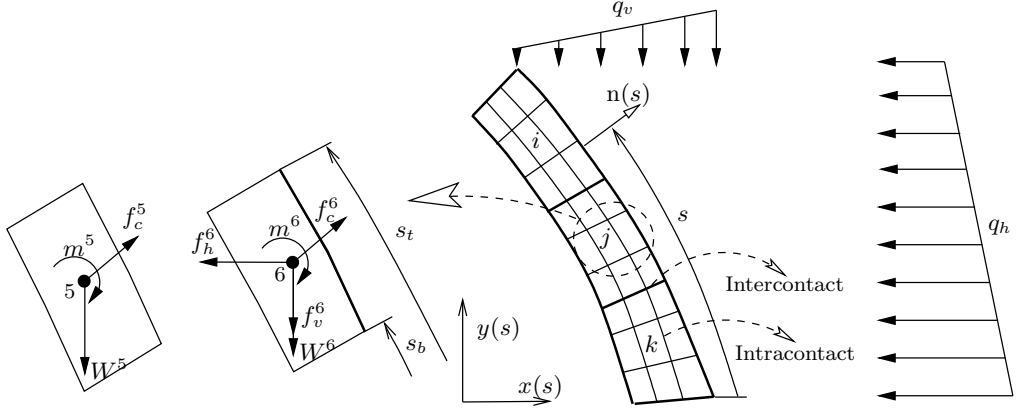
Figure 1: External and contact loads applied to the center of mass of subblocks, transferred from the extrados. Intercontact boundaries between stones (thick lines) and intracontact (internal, thin lines) inside each stone.

each block $i$ (see section 3 for the motion analysis of each block) provides the simultaneous equilibrium for a system of $N$ blocks:

$$\frac{\partial \Pi}{\partial \boldsymbol{D}} = \frac{\partial \sum_{i=1}^{N} H_i}{\partial \boldsymbol{D}} = 0 \rightarrow \underbrace{\begin{bmatrix} k_{11} & k_{12} & \ldots & k_{1N} \\ k_{21} & k_{22} & \ldots & k_{2N} \\ \ldots & \ldots & \ldots & \ldots \\ k_{N1} & k_{N2} & \ldots & k_{NN} \end{bmatrix}}_{\mathcal{K}} \underbrace{\begin{bmatrix} D_1 \\ D_2 \\ \ldots \\ D_N \end{bmatrix}}_{\boldsymbol{D}} = \underbrace{\begin{bmatrix} f_1 \\ f_2 \\ \ldots \\ f_N \end{bmatrix}}_{\boldsymbol{f}} \quad (1)$$

Eq. 1 (left) are assembled as in FEM providing a linear system, Eq. 1 (right); this system is composed of a stiffness matrix $\mathcal{K}$ with $N \times N$ submatrices each of dimension $n_{dg} \times n_{dg}$, and discretized load $\boldsymbol{f}$ and displacement vectors $\boldsymbol{D}$ each with $N$ terms of dimension $n_{dg}$.

## 3. Block modeling

The most common DDA formulation uses first order discretizations for the kinematic description; the movement is directly computed with the expression $\boldsymbol{x} = \boldsymbol{X} + \boldsymbol{U}$, where $\boldsymbol{X}$ represents its material coordinates and $\boldsymbol{x}$ the spacial ones. The vertical and horizontal displacements at any point of the block are discretized as $\boldsymbol{U} = \boldsymbol{TD}$. The linear operator $\boldsymbol{T}$ modifies the vector $\boldsymbol{D}$ that contains the following six degrees of freedom: two displacements, one rotation and three strains all of them applied at the center of masses $(CoM)$ of the block. The stresses and strains are therefore constant through the block; although a relatively small number of blocks is necessary to properly capture the movement of the blocks, a high number will in general be required to simulate the elastic fields.

### 3.1. Internal and external loads

Fig. 1 shows an schematic representation of three $i, j, k$ contacting macroblocks divided into nine subblocks each (see next subsection) under variable horizontal $q_h$ and vertical $q_v$ external, distributed loads. For the subblocks that are in direct contact with the distributed loads (on the extrados or external curved side in this work), statically equivalent point forces $f_h^e, f_v^e$ and the corresponding moment $m^e$ applied on the $CoM$ are calculated with

$$f_h^e = \int_{s_b}^{s_t} q_h(s) \ \mathrm{d}y(s) \ ; \qquad f_v^e = \int_{s_b}^{s_t} q_v(s) \ \mathrm{d}x(s)$$

(2)

$$m^e = \sum_n r_c^n \times f_c^n + r_h^e \times f_h^e + r_v^e \times f_v^e$$

9

where $s$ is a curvilinear coordinate starting at the arch bottom, $s_b$, $s_t$ its values at the bottom and top corners (nodes) of the extrados and $dx(s), dy(s)$ the projected horizontal and vertical components of a differential length on the extrados, see Fig. 1. In the third expression, $r_c^n$ refers to the distance between the $CoM$ and each node $n = 1, \ldots, 4$ of the subblock, where the contact forces $f_c^n$ are computed. The distances $r_h^e$, $r_v^e$ are again from the $CoM$ but now to the application point of $f_h^e, f_v^e$, both of them on the extrados of the external subblock $e$, Fig. 2. It is important to remark that the forces $f_h^e, f_v^e$ are statically transferred to $CoM$ of the external subblock from its extrados adding the moment $m^e$.

In addition, for all subblocks the self weight $W^e$ and the resultant of the applied contact forces $f_c^n$ are also equivalently applied and translated to the $CoM$, respectively. The latter must again include the corresponding cross product, adding to the moment $m^e$. Notice that the contact forces are not in general perpendicular to the interfaces due to the tangential friction component.

## 3.2. Substructure technique

To replicate the physics of contact (dry or mortar) between stones or bricks, it seems reasonable to simulate each piece with a block, for instance to evaluate the behavior of arches with the same geometry and load but composed of an increasing number of stones. But taking into account the necessity of a high number of information points to simulate the stress field, a substructuring technique has been developed in this paper. This technique is schematized in Fig. 2: a rectangular block (called "macroblock") is internally divided into a number of rectangular subblocks, nine in this figure; each

10

subblock, with the same number of degrees of freedom as the original, is connected to the neighbors through modified contact algorithms.
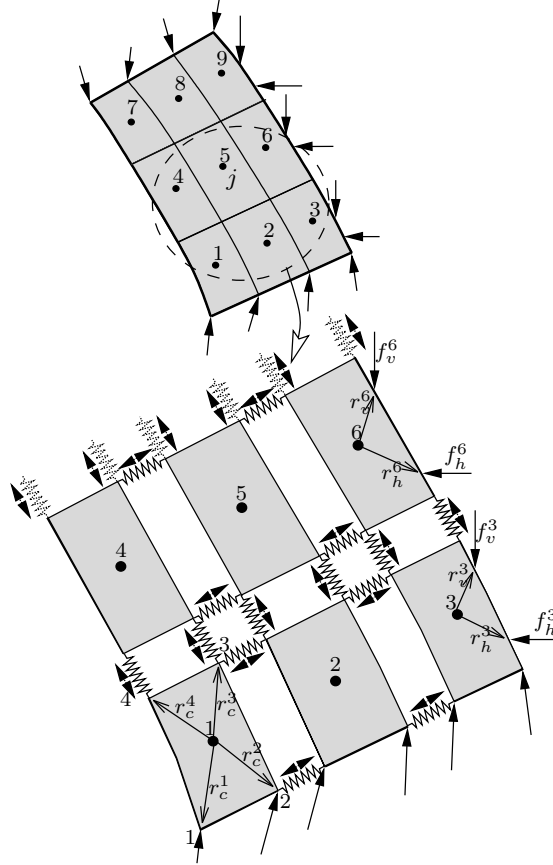


Figure 2: Substructuring a macroblock into subblocks to simulate a continuum. Contact forces between internal subblocks represented by double arrow; external forces (including contact from other macroblocks) by single.

The modification is defined by springs between each of the intracontact boundaries (see Fig. 1) in their normal and tangential directions. In this type of connections, and contrary to the standard contact algorithms, the interactions allow compression and tension forces to enforce both impenetra-

bility and attachment of the subblocks. Additionally, to avoid the relative displacement between subblocks, artificially high values of $\phi$ and $C$ are imposed. For intercontact boundaries, the standard penalty method is applied, allowing separation but not impenetrability. The relative displacement is here governed by the physical $\phi$ and $C$ of the material.

Action–reaction forces $f_c^n$ will appear at each internal node, while the perimeter of the macroblock will be subjected to contact from others and possibly to external forces. With this technique (similar to $h$–refinement) the complications of a high–order DDA formulation (similar to $p$–refinement) are avoided and a convergent stress field simulation can be obtained, due to the multiplicity of information at the $CoM$ of each subblock. The division into subblocks is not computationally expensive since contact search is avoided by an invariant (even during deformation or if necessary dynamic movement) allocation vector. Summarizing, the subblocks act like constant–strain finite elements hold together by the contact algorithm and the interfaces remain together to simulate the continuum.

The process to implement a macroblock in DDA is summarized as:

- Subdivide each block in a specified number of subblocks

- Define intercontact and intracontact boundaries

- Apply the modified penalty method to intracontact boundaries, with high artificial $\phi$ and $C$

- Apply the standard penalty to intercontact boundaries, with physical $\phi$ and $C$

*3.3. Validation*

In order to validate the substructure technique, a comparison of DDA and elasticity stress fields for a curved beam (similar to a continuous semi–arch) is developed in this subsection. The numerical results are obtained from a single macroblock discretized into a variable number of subblocks (from 4×4 to 16×16), while the theory of elasticity solution is taken from the classical reference [27]. The internal and external radii are $a = 0.5$ and $b = 0.7$ m respectively, the horizontal straight free surface is subjected to a flexural distribution $\sigma_\theta\left(r, \frac{\pi}{2}\right)$ with upward resultant $P = 2.5$ kN (see Fig. 3 top) and the vertical free surface to a parabolically distributed $\tau_{r\theta}(r, 0)$ also with resultant $P$ but downward, both according to the elasticity solution

$$\sigma_\theta\left(r, \tfrac{\pi}{2}\right) = \frac{P}{\Delta}\left[3r - \frac{a^2b^2}{r^3} - \frac{a^2 + b^2}{r}\right] \; ;$$

$$\tau_{r\theta}(r, 0) = \frac{P}{\Delta}\left[-r - \frac{a^2b^2}{r^3} + \frac{a^2 + b^2}{r}\right] \; ; \tag{3}$$

$$\Delta = a^2 - b^2 + (a^2 + b^2)\;\log\frac{b}{a}$$

Both distributions are in vertical equilibrium, therefore no essential boundary conditions are necessary. To facilitate the application of these external forces, two narrow stripes composed of 20 subblocks (bottom figure 3) are discretized at each free surface. Notice that no continuity between these "loading" subblocks and the "internal" ones is needed, thanks to the contact surfaces. The forces on each loading subblock side are proportional to the corresponding length of the distribution, and assumed applied at the point defined by the center of gravity of the subarea distribution; each force is then

13

translated to the *CoM* with the corresponding moment. The contact parameters for the internal subblocks are chosen so that no interpenetration or detachment are allowed: friction $35°$, normal and tangential penalty spring stiffness $1 \times 10^{10}$ N/m (see also section 4.1).

The equivalent stress is defined according to the Tresca criterium as

$$\sigma_{eq} = \max \left\{ \left| \sigma_I - \sigma_{II} \right|, \quad \left| \sigma_I \right|, \quad \left| \sigma_{II} \right| \right\} \tag{4}$$

where $\sigma_I$, $\sigma_{II}$ are principal stresses computed from the two–dimensional state of stress $\sigma_\theta$, $\sigma_r$, $\tau_{r\theta}$ with the usual tensorial notation. It is worth noting that the first component is one order of magnitude larger than the other two, therefore $\sigma_{eq} \approx \sigma_I \approx \sigma_\theta$ in most points. Also, $\sigma_r$, $\tau_{r\theta}$ are zero at $r = a, b$ and since the ratio $b/a = 1.4$ is small, the maximum of both appear at the center of the $r$ direction. Stresses $\sigma_\theta$, $\sigma_r$ are function of $\sin \theta$ in the circumferential direction, with maximum at the bottom end and zero at the top, while $\tau_{r\theta}$ is function of $\cos \theta$ with opposite maximum and minimum.

The $\sigma_{eq}$ calculated from DDA: $\sigma_{eq}^{dda} \big|_n$ and from elasticity: $\sigma_{eq}^{ely} \big|_n$, $1 \leq n \leq N$, are computed at the *CoM* of all subblocks. They are organized in vectors $\left\{ \sigma_{eq}^{dda} \right\}$ and $\left\{ \sigma_{eq}^{ely} \right\}$ with dimension $N$, where $\sqrt{N}$ denotes the number of subblocks along both the radial and circumferential directions. As mentioned, the distribution of $\sigma_{eq}$ is similar to that of $\sigma_\theta$ except close to $r = a, b$ and $\theta = \pi/2$ where $\sigma_\theta$ and $\sigma_r$ values add and subtract, respectively.

The error in percentage $e_N$ for a given mesh $N$ is defined as the euclidean norm of the difference between the two stress vectors.

14

$$e_N = 100 \frac{\left|\left|\{\sigma_{eq}^{ely}\} - \{\sigma_{eq}^{dda}\}\right|\right|_2}{\left|\left|\{\sigma_{eq}^{ely}\}\right|\right|_2}$$

$$= 100 \frac{\sqrt{\sum_{n=1}^{N} \left(\sigma_{eq}^{ely}\big|_n - \sigma_{eq}^{dda}\big|_n\right)^2}}{\sqrt{\sum_{n=1}^{N} \left(\sigma_{eq}^{ely}\big|_n\right)^2}} \tag{5}$$

A rate of convergence, [28], is calculated as the limit of the ratio between norms of two consecutive, doubled mesh sizes $e_{2N}$ and $e_N$:

$$\lim_{N \to \infty} \frac{e_{2N}}{e_N} = 1 \tag{6}$$

Fig. 4 shows the DDA convergence versus the number of subblocks (left ordinate). An approximated linear rate for $N \leq 100$ is obtained. Increasing the number of subblocks after that number produces only a small decrease of the error, implying a sublinear convergence. Only 5% error for a mesh of $N = 49$ subblocks and almost nil for $N = 100$ is observed. The CPU time in a standard portable personal computer is also plotted (right ordinate); notice that the 5% error is reached for a total computation time of only 4 s. The curve is parabolic since the computer code running time also is: the global matrix inversion is proportional to the cube of the mesh size and the managing of data and files is quadratic. Obviously a small error for this continuum problem would be obtained using the FEM with fewer elements and lower computational time, but the point is to validate a single method that studies instability through contacting blocks and internal stress fields at the same time.

15
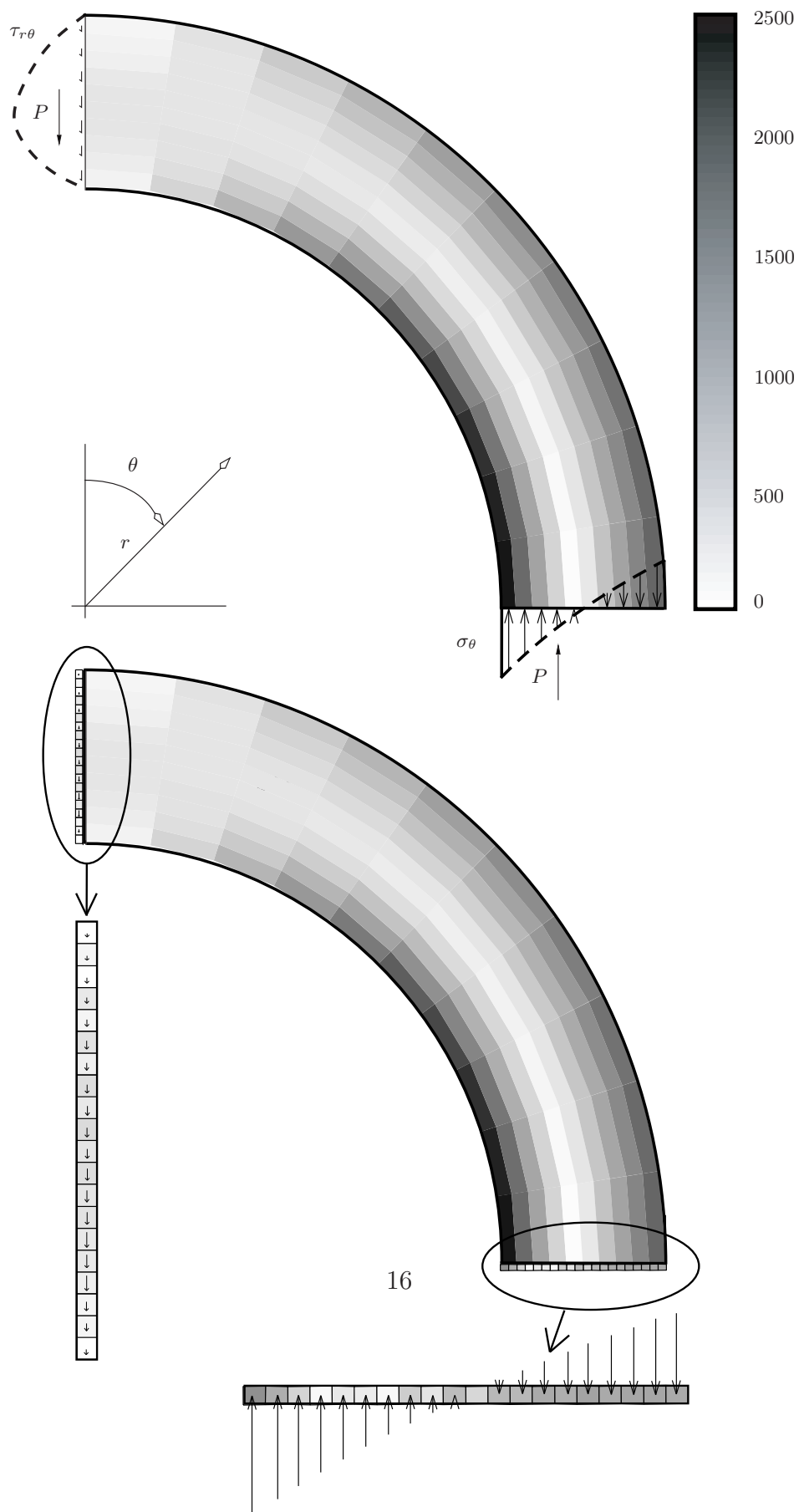
Figure 3: Tresca equivalent stress (N/m$^2$) distribution for a curved beam in bending: elasticity (top) and numerical (bottom, Discrete Deformation Analysis) results match closely
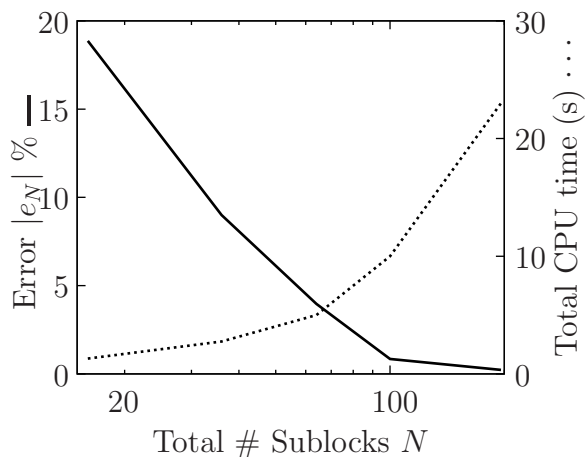
Figure 4: Error between Discrete Deformation Analysis and theory of elasticity results (left ordinate) and CPU time (right ordinate) vs. total number of subblocks.

## 4. Case 1: Buried arch under vertical load and filling

Experimental and numerical tests are described in this section for an arch (or vault) under the action of filling terrain and vertical, quasi–concentrated loads. The geometry, Fig. 5, corresponds to a buried arch whose thickness increases from the peak to the abutments (vertical lower blocks) and is supported on rigid foundations. The arch is assembled with direct contact among the stone blocks (dry masonry); stability is achieved through the curvature of the structure and the contact and friction generated by the asperities of the blocks. To facilitate the collapse, the arch does not mount keystone resulting in an even number of blocks.

The experimental testing program, [23], consisted on the crumbling of arches of equal dimensions but with different 9, 17, 27 and 61 of mobile (or active) joints. These arches are covered with soil on the extrados from the abutments to a height of 4.65 m (filling) and in addition two hydraulic jacks

17

apply quasi–concentrated vertical loads, see Fig. 5. The jacks are located symmetrically at distances 1.5 m and apply a total force in two areas $1.5 \times 1.0$ m$^2$ that are directly transmitted to the adjacent blocks and increase the vertical thrust of the filling. All external loading is parameterized by an intensity $q_0$ (force per unit length): each jack direct force results in $1.675 q_0$ and the filling thrust is represented by three stages of quasi–hydrostatic load with decreasing intensities 0.7, 0.6 and $0.5 q_0$.
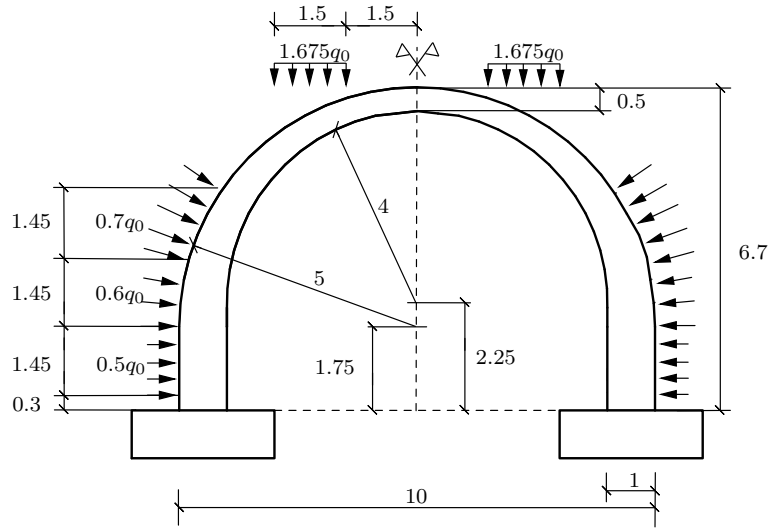


Figure 5: Symmetric buried arch: geometry (dimensions in m) and parameterized loads from [22].

Results for an arch with 201 joints are also reported in the reference, but this configuration has not been simulated since the critical loads and failure mechanisms are nearly the same as those of the 61–joint arch.

## 4.1. DDA numerical data

The shape and dimensions of the arch were estimated from a figure in the reference, resulting in Fig. 5. Then, the complete perimeter is divided into $J$ active joints and each abutment and block is simulated by a rectangular macroblock of only one subblock, since the reference provides for this case collapse due to instability and not to compression. The foundations are represented by an additional rigid rectangular block prevented from moving; these restraints are the only essential boundary conditions. The two joints between abutment and foundation are considered fixed. The rigid body motions of the arch are prevented by contact and friction between blocks, according to the Kuhn–Tucker conditions, [25].

The blocks are considered of high stiffness: Young modulus $E = 1 \times 10^9$ N/m$^2$ was chosen to be high enough to enforce rigidity but not to interfere with computer precision. The Poisson's coefficient is the standard $\mu = 0.25$. As for contact parameters, a friction angle for dry masonry of $\phi_s = 30°$ and no cohesion were reported. The penalty parameter is the stiffness of the elastic contact springs; the usual $\epsilon_N = 1 \times 10^{10}$ N/m was used, greater than $E$ to enforce that penetrations between blocks are lower than displacements related with strains. The self weight of the arch is calculated from a density $\gamma_s = 2300$ kg/m$^3$. The filling is considered to be gravel with density $\gamma_f = 1600$ kg/m$^3$, friction angle $\phi_f = 30°$ and no cohesion. In addition to the jack loads (present only in a few blocks close to the peak) that contribute to $q_v$, the hydrostatic loads from this filling contribute to both $q_v$, $q_h$, see (7) below. Table 1 summarizes the material properties for this case and for most properties of the following cases.

| Property | Value | Units |
|---|---|---|
| Stone Young's Modulus $E$ | $1 \times 10^9$ | N/m$^2$ |
| Stone Poisson's coeff. $\mu$ | 0.25 | [-] |
| Stone density $\gamma_s$ | 2300 | kg/m $^3$ |
| Stone strength (compr) $\sigma_u$ | $1 \times 10^7$ | N/m$^2$ |
| Stone friction $\phi_s$ | 30° | |
| Stone cohesion $c$ | 0 | N/m$^2$ |
| Filling density $\gamma_f$ | 1600 | kg/m$^3$ |
| Filling friction $\phi_f$ | 30° | |

Table 1: Material properties for stone and filling.

*4.2. Numerical results*

Due to the parametrization of the external loads, $q_0$ is the main unknown to reach collapse. This intensity is found by iteration with several runs of the computer code. Starting from zero, the load is increased by steps of five kN until collapse is predicted. The arch caves in by instability when several symmetric hinges form close to the abutments, close to the peak and at other locations and when contact is lost in one or more blocks. The failure criteria for hinge formation is considered fulfilled when the separation of two contiguous nodes is larger than a user–chosen critical distance (0.01 m in the current calculation). The hinge positions themselves are the other important result of the computations.

Once it is decided that initial collapse (failure) is reached, the corresponding $q_0$ is kept constant and successive DDA iterations simulate the initial
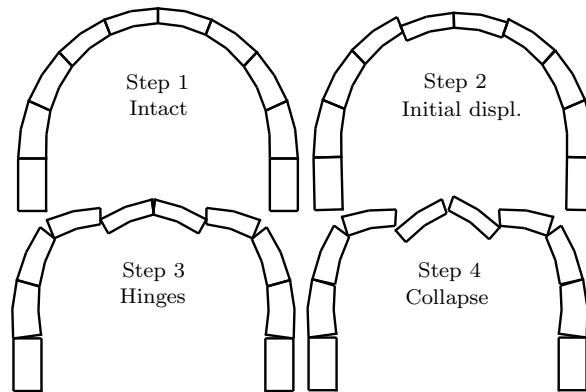
Figure 6: Collapse sequence for arch with 9 joints, Fig. 5.

collapsing process. Fig. 6 shows the sequence for a 9–joint arch. The first step represents the configuration just when failure starts. The second shows the initial displacements; given the relative high force of the jack, they appear mainly in the upper two blocks with a significant sliding. In the third step, sliding is replaced by rotations, and symmetric hinges appear close to the abutments and to the peak in the first and second blocks (from the top, both directions). It is clear that the arch "opens" to the sides mostly due to rotation of the lower hinges. Finally, in the fourth step the two upper blocks separate and drop due to lack of friction restraint. Since the loads are applied very slowly, the computation is static (no inertial forces are considered) and therefore valid only for the initial steps of the collapse. As well know by architects, the hinges alternate: along the circular line of the arch an external hinge follows an internal one or vice versa. The same situation will repeat for the following cases.

In Fig. 7, the second step is shown for arches with 17 and 27 joints. In the left we can observe a block displacement pattern similar to that of Fig. 6,
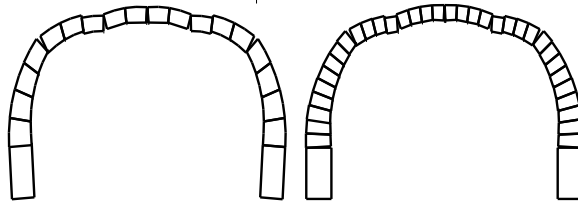
Figure 7: Initial failure (Step 2) for arches with 17 and 27 joints, Fig. 5.

including the length of the descending top portions and the position of the hinges. Some asymmetry can be observed in both cases, since the contact algorithms produce small bifurcations during the simulation. This effect is important for the corner-to-corner contact; far from being detrimental it is often very useful to obtain averaged results, more realistic than those from the purely deterministic simulations.
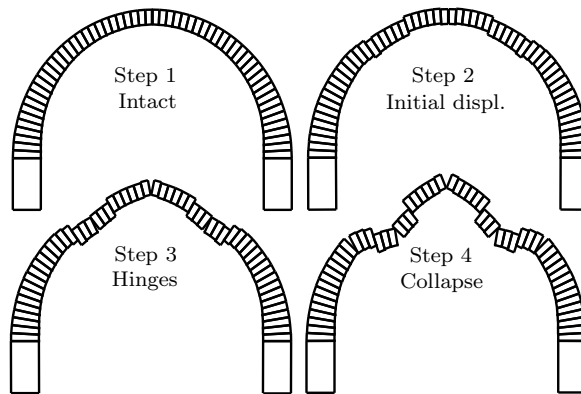


Figure 8: Collapse sequence for arch with 61 joints, Fig. 5.

Finally, Fig. 8 shows the collapse sequence of an arch with a large number of joints (61). Here, symmetry was forced by analyzing only half of the arch and prescribing zero friction for the top block, in contact with a rigid vertical surface. In this configuration the effect of the vertical loads is mostly local

both at right and left of the peak, where blocks below the jack descend at each side. Due to the high number of blocks and therefore contacts, the hinges are not very clear (except close to the peak) until the last step is reached: friction between the contact sides of the blocks prevents excessive movement up to collapse. Due to the discontinuity produced by the jack action, the arch opens in its middle, while the global vertical movement of the peak more or less compensates the inward horizontal thrust. The structure behaves more like a chain than as an arch, therefore, the effects are mostly local. For instance, there is no lateral expansion, since the upper blocks descend rather than rotate.

In Table 2 experimental and numerical results corresponding to the critical point loads for the different configurations are presented.

| # joints | Critical load experiment | Critical load DDA | Error % |
|----------|--------------------------|-------------------|---------|
| 9 | 250 | 280 | 12.2 |
| 17 | 206 | 210 | 1.6 |
| 27 | 206 | 205 | -0.8 |
| 61 | 205 | 205 | 0.1 |

Table 2: Experimental and numerical results. Critical intensity load $q_0$ in kN/m vs. number of joints for arch in Fig. 5.

Notice that when the number of joints increases the critical load tends to an asymptotic value. This result is well known in architecture and represents the fact that, when the arch has many blocks and consequently many joints, more weak points that permit the turning or sliding of the blocks ex-

its. References such as [10] have reported this tendency with discontinuous numerical and special finite element methods, but without validating their results with experiments. We can also observe that the error is reduced substantially when the problem involves a large number of joints. This is due to the solution being less sensitive to uncertainties in the data when multiple possible failure modes can be captured by DDA; as in any converging numerical method, the solution is better when the number of elements is higher. Finally the implemented kinematics are of first order, meaning that for large blocks precision in the movements is somewhat lost.

## 5. Case 2: Influence of embankment thickness on oval arch stability

Numerical simulations of the second experimental arch from [22] are presented in this section. Again geometry (now of oval shape) and loads are estimated from the reference, see Fig. 9. Macroblocks are discretized into four subblocks in the radial direction $r$ and in the in circumferential $s$, all of them of approximately constant length. The lateral thrust from the filling is still present, but instead of the jack vertical forces a distributed load from an embankment of variable thickness $h_e$ is considered.

The arch can be unstable for two reasons (see Fig. 12):

- The lateral thrust of the filling dominates over the vertical loads when $h_e$ is low; collapse occurs by elevation of the peak and formation of hinges, top figure

- The vertical forces are prevalent when $h_e$ is high; collapse occurs by descent of the peak and again hinge formation, bottom figure

24
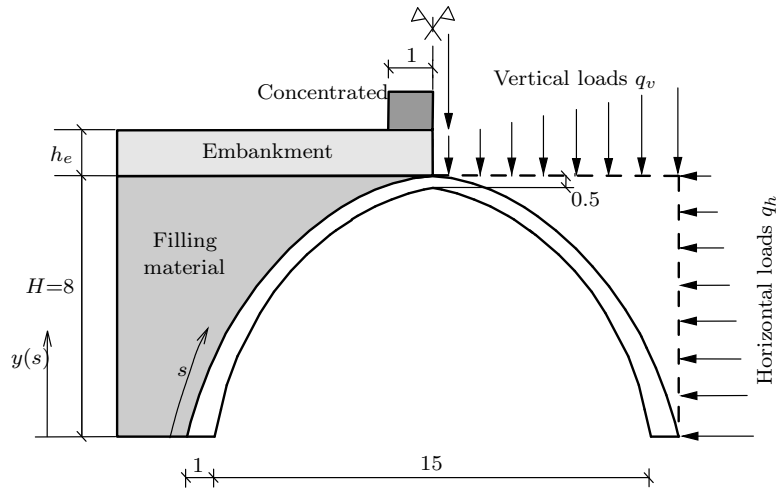
Figure 9: Scheme from [22] of a symmetrical oval arch (dimensions in m) and external loads from embankment and filling materials and from concentrated load. Materials substituted by corresponding forces in the right symmetric part.

Therefore there is an optimal range in the thickness of the embankment that stabilizes the arch.

The arch is simulated with 16 blocks, the two lowest simply supported on the foundations so that they can rotate or translate. The situation is similar to that of the previous case except for the geometry and the vertical external loads, aspects that produce different failure modes.

Two experimental collapses are described in the reference. One corresponds to the first item before: absence of enough vertical load and ruin due to lateral thrust, defined as *lower limit*. The same arch is then tested with increasing $h_e$ until a new collapse is caused by excessive weight (second item), defined as *upper limit*. For both collapses lateral hinges open alternately (towards the intrados or the extrados) for the two limits. For the upper limit, the rotations at the base cause the lower blocks to partially lose contact with

25

the base. An intermediate failure is also defined from a standard compression test (stress $\sigma_u$) of the stone.

From simple funicular polygons and strength of materials equilibrium similar to that proposed by [1], [22] calculates the continuous line (between lower and upper limits) drawn in Fig. 10, differentiating between two instability modes and failure by compression. Starting from the lower limit, $h_e = 0.32$ m and therefore safety factor $SF = 1$, the calculation fixes $h_e$ but increases in steps and proportionally the loads $q_h$, $q_v$ from (7) and draws the corresponding funicular polygons, obtaining a $SF$ for each load level. The safety factor is defined from 1 to $\infty$ and the abscissa is a function of the representative $h_e$. After the lower limit, a linear distribution up to $h_e = 0.9$ m with high slope is observed, implying that a small increase in load greatly increases the safety of the structure (zone I). After I, an increasing/decreasing short zone (with maximum in the optimal $h_e = 1.9$ m) corresponds to failure by block compression (zone II); this failure is visualized with the funicular polygon being inside the arch. When the loads increase even more, there is a progressive decrease in safety (zone III) due to excessive weight until failure is again reached for $h_e = 11.9$ m, upper limit.

### 5.1. Numerical computation with DDA

The safety factors of the oval arch are calculated with DDA. The loads produced by the self weight are computed directly from the volume and material of each block defined in the previous section. For filling, the same values are also used, but taking into account the reported compaction, an increase of 10% is considered for low thicknesses, with a final value $\gamma_e = 1760$ kg/m$^3$. For high thicknesses, $h_e > 1.9$ m, the value from the reference is used

26

since compaction often is much less effective.

Fig. 1 schematizes the loads that act on the macroblocks: besides contact and weight point loads, the actions of filling and embankment are represented. These vertical and horizontal actions are calculated with the following equation from [29]

$$q_v(s) = [H - y(s)] \, g \, \gamma_f + h_e \, g \, \gamma_e$$

$$(7)$$

$$q_h(s) = (1 - \sin \phi_f) \, q_v(s)$$

where $g$ is the gravity acceleration. The total filling height $H$ and the variable height $y(s)$ are depicted in Fig. 9. The actions are transformed into point forces simply multiplying them by the horizontal and vertical projections of the external side of the block, and the resulting point loads and corresponding moments are then applied to the $CoM$.

With the DDA model and by trial and error, the lower and upper limits that stabilize the arch are computed, finding $h_e = 0.5$ m and 12 m, very close to the experimental ones. As in the reference but automatically, for particular values of $h_e$ the program increases the values of both $q_h(s)$, $q_v(s)$ until collapse occurs when three or more hinges are formed with the criteria mentioned in section 4.2. At the same time the maximum equivalent stress is compared with $\sigma_u$, calculating the corresponding $SF$ from instability or from compression. In the transition between the two instabilities (zone II) the line of application of the forces' resultant crosses the central core of all sections, close to the center of gravity. Therefore the block is subjected to almost no turning moment, only compressions are present and hinges are not formed. In this situation, the only possible failure is by elastic compression

when the maximum equivalent Tresca stress $\sigma_{eq}$ (see (4)) equals the failure compression stress of the stone $\sigma_u$. In Fig. 10, the distribution of $SF$ from numerical results is represented with ticks; given the uncertainties in the data the general agreement between these and the experimental one is very good.
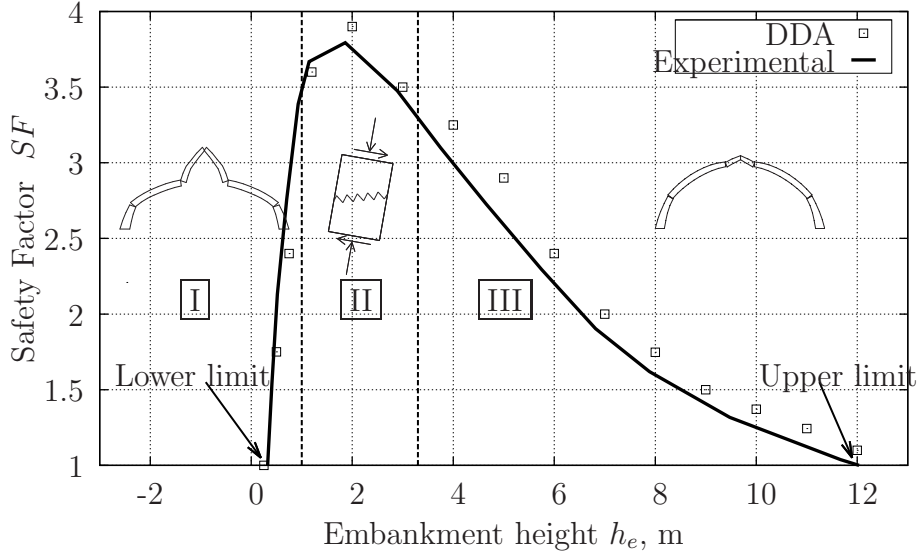


Figure 10: Safety factors vs. embankment thickness $h_e$ for experimental and numerical (Discrete Deformation Analysis) for oval arch (Fig. 9). Failure by: I instability, peak raising; II elastic compression; III instability, peak descent.

To visualize the numerical stress distribution, Fig. 11 shows the equivalent Tresca stress when $h_e = 2$ m, that is, in the center of zone II in which failure occurs by compression. The range from 7.2 to 9.2 Mpa indicate that as expected the oval arch is subjected to a more or less constant stress. It is also clear that concentrations occur at the arch peak, at the middle and by the abutments, the three of them alternating on the intrados and the extrados. These concentrations are due to the addition of bending moments and compressive forces, and coincide approximately with joints in which hinges

are formed, see Fig. 12. But it is important to remark that DDA does not directly predict the hinge formation by the stress level, but displacements and rotations do. The actual point in which compression failure would occur is the lower concentration for which $q_v = 160.1 - 0.15y$ kN/m and $q_h = 0.5\ q_v$ kN/m augmented by $SF = 3.8$.
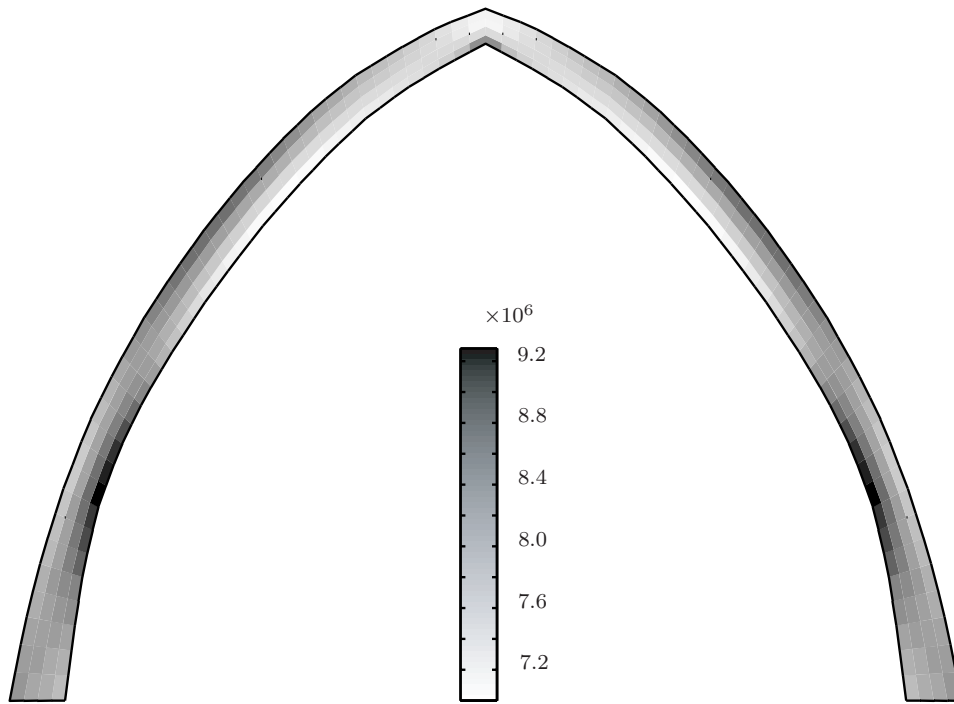


Figure 11: Tresca equivalent stress distribution (N/m$^2$) for the oval arch of Fig. 10 and embankment $h_e = 2$ m.

The second comparison between experimental and numerical results is related to the failure modes of the oval arch; Fig. 12 shows the predicted collapse. For the lower limit of embankment thickness (top figure), it is evident that the lateral forces are prevalent and that the peak rises; due to symmetry, a hinge tends to open in the peak towards the extrados. Two

| Limits | Numerical | | | Experimental | | |
|--------|-----------|-----|-----|--------------|-----|-----|
| Lower | 18° | 60° | 90° | 18° | 60° | 90° |
| Upper | 0° | 26° | 78° | 0° | 37° | 78° |

Table 3: Comparison of hinge angles vs. embankment thickness $h_e$: low $h_e$ for lower limit, high $h_e$ for upper limit.

other hinges on each side open alternately, the first one towards the intrados. For the upper limit (bottom figure) DDA predicts just the contrary: due to the embankment weight, the prevalent load is vertical; the peak descends and again two alternate hinges open.

The experimental (from [22]) and numerical angles of these hinges are shown in Table 3. These angles refer to the initial configuration, that is, during the initial steps of the collapse. It is worth noting that all angles are very close, with the exception of the intermediate angle for the upper limit. This difference is due to the almost verticality of the block between joints at 26° and 37°: a small variation of the experimental data may provoke the creation of a hinge in one or other consecutive joints.

## 6. Case 3: Influence of concentrated load on oval arch stability

The oval arch from the previous section is studied under the same conditions except for the addition of a vertical load. This new load is concentrated at the peak and exerted through a single jack that applies a load intensity per unit depth $q_p$ distributed on a rectangle of dimension $2 \times 1$ m. The width of the load distribution covers approximately one block at each side of the peak,

30
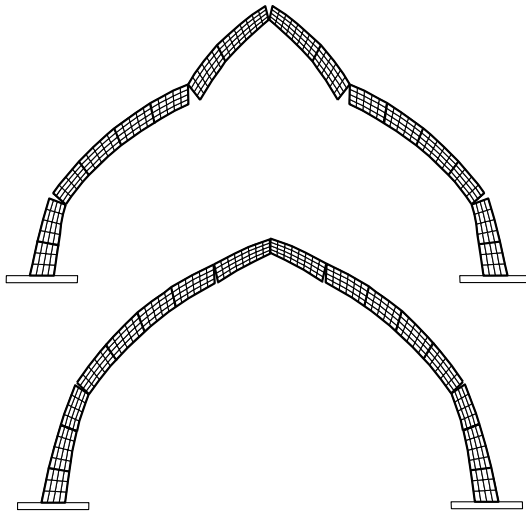
Figure 12: Case 2: DDA collapse of fifteen–joint oval arch (Fig. 9) for: lower limit (top) by peak raising; upper limit (bottom) by peak descent. Thick line for macroblocks, thin for subblocks.

and its effect is directly translated to the corresponding $CoM$. The embankment has now a small constant thickness $h_e = 0.2$ m (corresponding to the lower limit of the previous case), therefore it is considered well–compacted with a high density $\gamma_e = 1760$ Kg/m$^3$. The rest of material properties and geometry are given in Table 1.

The objective is again to study the $SF$, but now versus concentrated intensity $q_p$; the procedure is the same as before, but $q_h$, $q_v$, and $q_p$ are augmented at the same time to calculate the $SF$.

Fig. 13 shows the comparison between experimental and numerical results, with similarities with Case 2: at a lower and an upper limit of the load the arch collapses, although under different instability modes. Notice that since the chosen embankment already produces instability, the lower limit is reached for $q_p = 0$; for any increase stability is immediately achieved. By

31
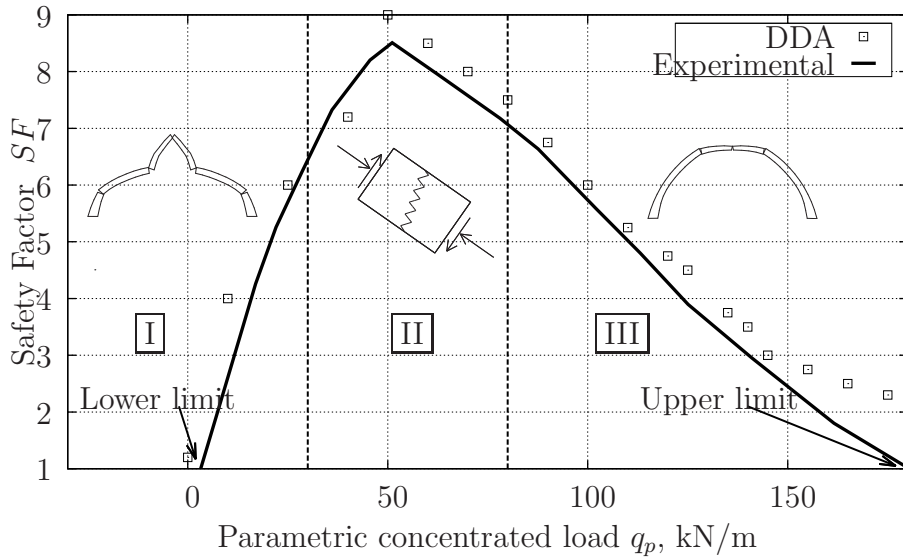
Figure 13: Safety factors vs. equivalent concentrated load for experimental and numerical (Discrete Deformation Analysis) for oval arch (Fig. 9). Failure by: I instability, peak raising; II elastic compression; III instability, peak descent.

varying $q_p$, we find that DDA predicts lower and upper limits of 2.5 and 225 kN respectively. The agreement between experimental and numerical results is again very good, except for $q_p > 150$ kN/m, for which DDA diverges predicting significant higher loads. This divergence could be due to the concentration of the vertical load in a few subblocks, producing a possible error in their translation and rotation. A more refined mesh generated in this area would solve the problem, but again this deviation is not an important issue for the simulation.

In Fig. 14, the failure modes corresponding to the lower and upper limits are shown. The mode corresponding to the lower limit is exactly the same as that of Case 2, due to the the equality of lateral loads and the vertical loads playing a marginal role. The positions of the hinges are compared in Table

4 with no significant error. The failure mode for the upper limit is different than before: four blocks at each side of the peak descend together, and only one internal hinge opens to the extrados. In this hinge a combination of friction and rotation is present, but the rest of the arch is unaffected by the vertical loads, moving just slightly inwards due to the lateral loads from the filling.
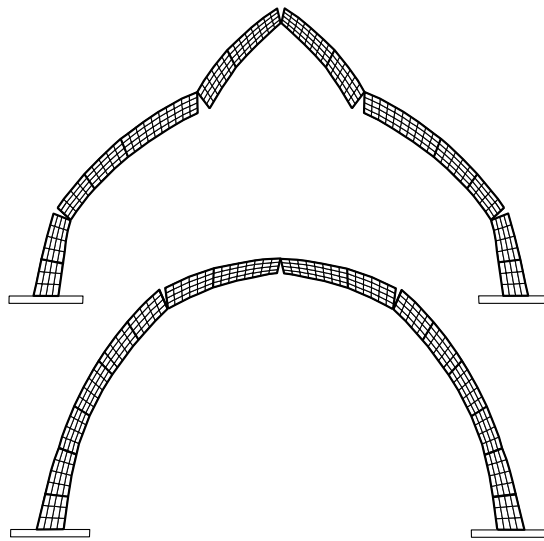


Figure 14: Case 3: DDA collapse of oval arch (Fig. 9) for: lower limit (top) by peak raising; upper limit (bottom) by peak descent. Thick line for macroblocks, thin for subblocks.

For cases 2 and 3 it is evident that for collapse friction plays a very small role and most of the movement is induced by the rotation of series of blocks. Due to the inclination of the arch sides, no much lateral movement occurs except of a slight motion for the upper limit, which creates a hinge in the base. The qualitative motions (movement of the peak, direction of the rotations) are the same as those given by the experiments.

| Limits | Numerical | | | Experimental | | |
|--------|-----------|------|------|--------------|------|------|
| Lower  | 18°       | 60°  | 90°  | 18°          | 60°  | 90°  |
| Upper  | 0°        | 63°  | 90°  | 0°           | 63°  | 90°  |

Table 4: Hinge angles vs. vertical concentrated load. Lower limit for collapse smallest load, upper for largest.

## 7. Conclusions

Several experiments taken from the literature have been simulated using the numerical method Discrete Deformation Analysis (DDA) and a specifically written computer code. This method is better suited for the analysis than continuous ones, since their discretization and formulation are much closer to the physical response of the problem. In addition the development, implementation and computational time are smaller. Three cases for two different arches are presented. The first is related to the resistance of a circular arch versus the number of joints, which as already known is asymptotic. The other two, study the resistance of an oval arch under distributed and concentrated loads. Some of the parameters of the problem (geometry etc.) were taken from the reference but others had to be estimated from other sources or by best guesses.

The failure modes as well as the limit parameters are well simulated by the numerical method for most cases. The analysis not only tackles failure by instability but also by compression. For that, the original DDA blocks are subdivided into subblocks that are kept together by the modified contact algorithm preventing both penetration and separation. In this way, the exte-

rior of the blocks is considered rigid but the interior is an elastic continuum simulated with a large number of internal nodes, a good approximation for materials such as stone, brick etc. It is worth noting that the intrinsic high computational cost of contact mechanics is not reproduced in the subblocking technique, since contact search is avoided and iterations reduced.

Further work is currently being conducted to apply DDA to effects not tested in the experiments, such as foundation settlement, other concentrated load positions and seismic behavior. When the numerical tool is finished and validated, it could be an important aid for the optimal design of real arches, vaults and domes, for which elevated safety factors are currently used.

## 8. ACKNOWLEDGEMENTS

**References**

[1] Heyman J. The masonry arch. Chichester: Ellis Horwood; 1982.

[2] MEXE . Military load classification of civil bridges by reconnaissance and correlation methods. Tech. Rep.; Military Engineering Experimental Establishment, Christchurch; 1963.

[3] 778-3R UC. Recommendations for the assessment of the load carrying capacity of existing masonry and mass-concrete arch bridge. Tech. Rep.; International Union of Railways; 1994.

[4] Pi YL, Trahair N. Three-dimensional nonlinear analysis of elastic arches. Engineering Structures 1996;18(1):49–63. doi:10.1016/0141-0296(95)00039-3.

[5] Casolo S, Peña F. Modelo de elementos rígidos para el análisis de estructuras de mampostería (rigid elements model for the analysis of masonry structures), in spanish. Revista Internacional Métodos numéricos para cálculo y diseño en ingeniería 2005;121(2):1–18.

[6] Towler K. The non-linear finite element analysis of bridgemill masonry arch bridge. Masonry International 1985;5:38–47.

[7] Crisfield M. A finite element method for a class of contact-impact problemsnite element computer program for the analysis of masonry arches. Tech. Rep.; TRRL Laboratory Report 1115, Department of Transport, Crowthorne; 1984.

[8] Zucchini A, Lourenço P. A micro-mechanical model for the homogenisation of masonry. International Journal of Solids and Structures 2002;39(12):3233–55. doi:10.1016/S0020-7683(02)00230-5.

[9] Zucchini A, Lourenço P. A coupled homogenisation-damage model for masonry cracking. Computers and Structures 2004;82(11–12):917–29. doi:10.1016/j.compstruc.2004.02.020.

[10] Drosopoulos G, Stavroulakis G, Massalas C. Limit analysis of a single span masonry bridge with unilateral frictional contact interfaces. Engineering Structures 2006;28(13):1864–73.

[11] Dolatshahi KM, Aref AJ. Two-dimensional computational framework of meso-scale rigid and line interface elements for masonry structures. Engineering Structures 2011;33(12):3657 –67. doi: 10.1016/j.engstruct.2011.07.030.

[12] Casolo S, Sanjust CA. Seismic analysis and strengthening design of a masonry monument by a rigid body spring model: The "maniace castle" of syracuse. Engineering Structures 2009;31(7):1447–59. doi: 10.1016/j.engstruct.2009.02.030.

[13] Bravo R, Perez-Aparicio JL. Discontinuous numerical analysis of masonry vaults; vol. 3. Berlin: Springer-Verlag Berlin; 2007, p. 365–80.

[14] Cundall P, Strack O. A discrete numerical model for granular assemblies. Geotechnique 1979;29:47–65.

[15] Rafiee A, Vinches M, Bohatier C. Modelling and analysis of the nîmes arena and the arles aqueduct subjected to a seismic loading, using the non-smooth contact dynamics method. Engineering Structures 2008;30(12):3457–67. doi:10.1016/j.engstruct.2008.05.018.

[16] Komodromos P, Papaloizou L, Polycarpou P. Simulation of the response of ancient columns under harmonic and earthquake excitations. Engineering Structures 2008;30(8):2154–64. doi: 10.1016/j.engstruct.2007.11.004.

[17] Dimitri R, Lorenzis LD, Zavarise G. Numerical study on the dynamic behavior of masonry columns and arches on buttresses with the dis-

crete element method. Engineering Structures 2011;33(12):3172–88. doi: 10.1016/j.engstruct.2011.08.018.

[18] Giordano A, Mele E, Luca AD. Modelling of historical masonry structures: comparison of different approaches through a case study. Engineering Structures 2002;24(8):1057 –69. doi:10.1016/S0141-0296(02)00033-0.

[19] Shi G. Discontinuous deformation analysis- a new model for the statics and dynamics of block systems. Ph.D. thesis; U.California, Berkeley; 1988.

[20] Munjiza A. Combined Finite-Discrete Element Method. Wiley & Sons; 2002.

[21] Pina-Henriques J, Lourenço P. Masonry compression: a numerical investigation at the meso-level. Engineering Computations 2006;23(4):382–407.

[22] Delbecq J. Casos de Puentes de Fábrica (Examples of masonry bridges), in spanish. SETRA; 1981.

[23] Delbecq J. Stability analysis of masonry arches by guild design method. Journal de Mecanique Theorique et Applique 1 1982;1(91).

[24] Gago AS, Alfaiate J, Lamas A. The effect of the infill in arched structures: Analytical and numerical modelling. Engineering Structures 2011;33(5):1450–8. doi:10.1016/j.engstruct.2010.12.037.

[25] Wriggers P. Computational Contact Mechanics. J. Wiley & Sons; 2002.

[26] Bravo R, Pérez-Aparicio JL, Laursen TA. An enhanced energy conserving time stepping algorithm for frictionless particle contacts. International Journal for Numerical Methods in Engineering 2011;85(11):1415–35.

[27] Timoshenko S, Goodier J. Theory of Elasticity. Mcgraw-Hill; 1951.

[28] Ostrowski AM. Solutions of Equations in Euclidean and Banach Spaces. Aca; 1973.

[29] Lambe T. Soil Mechanics. John Wiley & Sons; 1981.